

This work was written as part of one of the author's official duties as an Employee of the United States Government and is therefore a work of the United States Government. In accordance with 17 U.S.C. 105, no copyright protection is available for such works under U.S. Law.

Public Domain Mark 1.0

<https://creativecommons.org/publicdomain/mark/1.0/>

Access to this work was provided by the University of Maryland, Baltimore County (UMBC) ScholarWorks@UMBC digital repository on the Maryland Shared Open Access (MD-SOAR) platform.

Please provide feedback

Please support the ScholarWorks@UMBC repository by emailing scholarworks-group@umbc.edu and telling us what having access to this work means to you and why it's important to you. Thank you.



Noise reduction for solar-induced fluorescence retrievals using machine learning and principal component analysis: simulations and applications to GOME-2 satellite retrievals

Joanna Joiner^a, Yasuko Yoshida^b, Luis Guanter^c, Lok Lamsal^d, Can Li^a, Zachary Fasnacht^b, Philipp Köhler^{e,f}, Christian Frankenberg^g, Ying Sun^h, Nicolas Parazoo^e

^a *NASA Goddard Space Flight Center, Greenbelt, MD, USA*, ^b *Science Systems and Applications, Inc. (SSAI), Lanham, MD, USA*, ^c *Universitat Politècnica de València, València, Spain*, ^d *University of Maryland, Baltimore County, GESTAR, Baltimore, MD, USA*, ^e *Jet Propulsion Laboratory, Pasadena, CA, USA*, ^f *EUMETSAT, Remote Sensing and Products Division, Darmstadt, Germany*, ^g *California Institute of Technology, Pasadena, CA, USA*, ^h *Cornell University, Ithaca, NY, USA*

Corresponding author: Joanna Joiner, Joanna.Joiner@nasa.gov

1

Early Online Release: This preliminary version has been accepted for publication in *Artificial Intelligence for the Earth Systems*, may be fully cited, and has been assigned DOI 10.1175/AIES-D-23-0085.1. The final typeset copyedited article will replace the EOR at the above DOI when it is published.

© 2024 American Meteorological Society. This is an Author Accepted Manuscript distributed under the terms of the default AMS reuse license. For information regarding reuse and general copyright information, consult the AMS Copyright Policy (www.ametsoc.org/PUBSReuseLicenses).

ABSTRACT: We use a spectral-based approach that employs principal component analysis along with a relatively shallow artificial neural network (NN) to substantially reduce noise and other artifacts in terrestrial chlorophyll solar-induced fluorescence (SIF) retrievals. SIF is a very small emission at red and far-red wavelengths that is difficult to measure and is highly sensitive to random errors and systematic artifacts. Our approach relies upon an assumption that a trained NN can effectively reconstruct the total SIF signal from a relatively small number of leading principal components of the satellite-observed far-red radiance spectra without using information from the trailing modes that contain most of the random errors. We test the approach with simulated reflectance spectra produced with a full atmospheric and surface radiative transfer model using different observing and geophysical parameters and various noise levels. Resulting noisy and noise-reduced retrieved SIF values are compared with true values to assess performance. We then apply our noise reduction approach to SIF derived from two different satellite spectrometers. For evaluation, since the truth in this case is unknown, we compare SIF retrievals from two independent sensors with each other. We also compare the noise-reduced SIF temporal variations with those from an independent gross primary product (GPP) product that should display similar variations. Results show that our noise reduction approach improves capture of SIF seasonal and inter-annual variability. Our approach should be applicable to many noisy data products derived from spectral measurements. Our methodology does not replace the original retrieval algorithms; rather the original noisy retrievals are needed as the target for the NN training process.

SIGNIFICANCE STATEMENT: The purpose of this study is to document and demonstrate a machine learning algorithm that is used to effectively reduce noise and artifacts in a satellite data product, solar-induced fluorescence (SIF) from chlorophyll. This is important because SIF retrievals are typically noisy, and the noise limits its ability to be used for diagnosing plant health and productivity. Our results show substantial improvement in SIF retrievals that may lead to new applications. Our approach can be similarly applied to other noisy satellite data products.

1. Introduction

Many works have been devoted to reducing noise and artifacts in satellite data using spatial- and spectral-based approaches. Random and systematic errors in satellite Earthshine radiance observations arise from quantization, shot noise, and dark currents. These errors can limit the usefulness of satellite-derived products for science and applications. Efforts to denoise hyperspectral imagery (HSI) have evolved from two dimensional (2D) spatial approaches applied to individual bands to three dimensional (3D) methods that consider the spectral dimension using techniques such as wavelet and low-rank modeling (see e.g., the review of Rasti et al. 2018). Machine learning (ML) methods, including convolutional neural networks (NN), have also been employed to denoise HSI (e.g., Wang et al. 2022). There has been less documented research with purely spectral methods that differ from spatial noise reduction techniques reviewed by Thakur et al. (2021).

Our work focuses on reduction of noise and other artifacts in downstream satellite products that are retrieved using observed radiance spectra. Joiner et al. (2023) suggested the use of ML along with principal component analysis (PCA) of radiance spectra for noise reduction in retrieved satellite-based nitrogen dioxide (NO_2) slant column densities (SCDs). Their hypothesis was that ML models can reproduce spatio-temporal characteristics of noisy retrievals with acceptable performance using coefficients of a limited number of leading principal components (PCs) of the observed spectral radiances as input features. By eliminating coefficients of trailing PCs that primarily contain random noise, ML models are unable to reproduce noise in the retrievals. Joiner et al. (2023) applied their approach directly to actual NO_2 retrievals for which true values were unknown. Their method was evaluated using retrievals in an area where the target values were expected to have low variability.

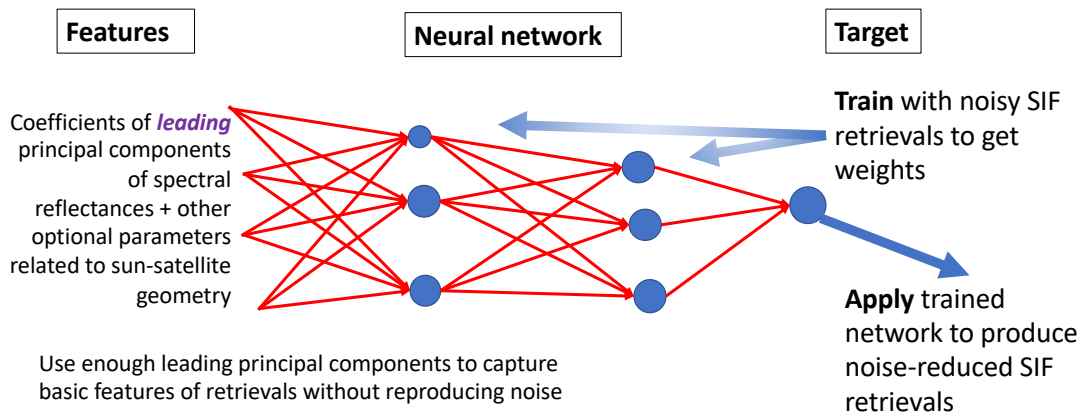


FIG. 1. Conceptual diagram of the noise reduction technique described by Joiner et al. (2023).

Here, we apply a similar approach to satellite-derived solar-induced fluorescence (SIF) retrievals that suffer from relatively low signal levels as compared with retrieval noise. SIF from chlorophyll-a in terrestrial vegetation can be measured using satellite-, aircraft-, and ground-based spectrometers (see e.g., the review of Mohammed et al. 2019). There are many potential applications of SIF measurements in the fields of ecology, precision agriculture, hydrology, climate feedback, and socioeconomics (see e.g., the reviews of Porcar-Castell et al. 2021; Sun et al. 2023b,a, and references therein).

A conceptual framework of noise reduction discussed by Joiner et al. (2023) as applied to SIF retrievals is laid out in Figure 1. The leading PCs (or eigenvectors) of near-infrared (NIR) radiances contain information about geophysical features in the Earth's surface and atmosphere, such as water vapor absorption. These features are present in every spectrum and explain a large fraction of spectral variability within any sample of spectra. For example, > 99% of NIR spectral variability is captured by a handful of leading PCs (Joiner et al. 2013). Random noise in satellite measurements is typically spread out across a large number of trailing PCs, and these PCs explain only a small fraction of total spectral variability. Our hypothesis is that the SIF spectral signature is presumed to be present primarily in the leading PCs such that a NN can reconstruct the SIF retrieval with only the coefficients of the leading PCs and without propagating the noise contained in the trailing PCs. Our approach can be classified as a purely spectral noise reduction method. As explained in more detail below, our ML method is better able to reconstruct SIF retrievals and reduce noise as compared with retrievals performed with reconstructed radiances that use leading

PCs to reduce noise. In short, the small SIF signal in real satellite spectra is spread out over a large number of PCs. This large spread leads to biases and marginal noise reduction in retrievals performed with reconstructed radiances.

Satellite SIF retrievals have relied upon the filling-in of solar Fraunhofer features in the Earth's backscattered reflectance spectra from SIF emission (Joiner et al. 2011; Frankenberg et al. 2011a; Joiner et al. 2013; Guanter et al. 2015; Köhler et al. 2015b, 2018b). Most retrievals have focused on SIF at the far-red emission feature that peaks near 740 nm. The retrieval spectral fitting window for SIF may contain atmospheric absorption features, such as from oxygen (O_2) or water vapor (H_2O). This absorption can be accounted for using a data-driven method that relies on analysis of spectra over fluorescence-free scenes (Joiner et al. 2013, 2016). The retrieval in this case is non-linear and requires an iterative solution. If a small spectral fitting window is used for which atmospheric absorption is small and can be neglected, the retrieval can be simplified (Joiner et al. 2011; Frankenberg et al. 2011a; Köhler et al. 2018b). For example, a linear regression can be used where instrumental artifacts and small absorption features can be fit simultaneously with spectral features associated with SIF and surface reflectance.

In this work, we consider only retrievals of far-red SIF emission near 740 nm that make up the vast majority of terrestrial SIF data products. Far-red SIF retrievals have been performed with spectrometers designed for greenhouse gas (GHG) retrievals including the Thermal And Near-infrared Sensor for carbon Observation Fourier Transform Spectrometer (TANSO-FTS) flying on the Greenhouse gases Observing SATellite (GOSAT) (Joiner et al. 2011; Frankenberg et al. 2011; Guanter et al. 2012; Köhler et al. 2015a), the Orbiting Carbon Observatory 2 (OCO-2) on a free-flying satellite, OCO-3 mounted on the Japanese Experiment Module-Exposed Facility International Space Station (ISS) (Sun et al. 2017, 2018; Doughty et al. 2022), and the Atmospheric Carbon dioxide Grating Spectrometer (ACGS) aboard the Chinese Carbon Dioxide Observation Satellite (TanSat) (Du et al. 2018; Yao et al. 2022). The high spectral resolution of the GHG sensors, with coverage in the O_2 A band for characterization of cloud and aerosol impacts on photon path length, enables the simpler linear approaches to SIF retrievals. Moderate-spectral resolution spectrometers, designed to measure trace-gas pollutants, typically have a broader spectral range that can be used to retrieve SIF with non-linear retrieval approaches. Such instruments include the Global Ozone Monitoring Experiment 2 (GOME-2) sensors that fly on the European METerology

SATellite (EUMETSAT) MetOp series (Joiner et al. 2013; Sanders et al. 2016; van Schaik et al. 2020), the GOME instrument on the European Space Agency's (ESA) European Remote Sensing satellite 2 (ERS-2) (Joiner et al. 2019), and the SCanning Imaging Absorption spectroMeter for Atmospheric CHartographY (SCIAMACHY) on the European Space Agency (ESA) Environmental Satellite (Envisat) (Köhler et al. 2015b; Khosravi et al. 2015). The TROPOspheric Monitoring Instrument (TROPOMI) on the Copernicus Sentinel-5 Precursor (S-5P) satellite has moderate spectral resolution with a higher sampling rate and achieves good performance with a linear SIF retrieval (Köhler et al. 2018b; Guanter et al. 2021). Several of these data sets are being harmonized to form long-term SIF records (Parazoo et al. 2019; Doughty et al. 2022).

Individual far-red SIF retrieval errors are typically of the same order of magnitude as the peak emission strength. SIF retrievals thus have much lower signal to noise ratios (SNRs) as compared with many other satellite-derived data products. Due to the relatively large retrieval errors, individual SIF retrievals are typically aggregated in time and/or space for scientific studies (e.g., Köhler et al. 2018). For example, in order to examine the dependences of sun-satellite geometry on SIF retrievals, substantial spatio-temporal averaging was applied (e.g., Joiner et al. 2020). It has not yet been possible to estimate parameters related to the spatio-temporal varying bi-directionality of SIF as has been done for reflectances (e.g., Lyapustin et al. 2011a,b, 2012; Schaaf et al. 2002).

Here, we test our hypothesis that a NN model can reproduce spatio-temporal characteristics of noisy SIF retrievals using a limited number of leading PCs of NIR radiance spectra, thus enabling noise reduction. We first apply our ML noise reduction approach to simulated spectra under a variety of scenarios for which true SIF values are available. In this controlled testbed, we can vary the SNR of the simulated observations. Results are assessed by comparing retrieved with true SIF values. We then apply our methodology to SIF retrievals from GOME-2 instruments aboard two MetOp satellites. The training is completely independent of the simulation data and can account for instrument specific artifacts. Because the true SIF is not known with the GOME-2 satellite retrievals, we assess the results by comparing retrievals from two different satellites. We also compare SIF variability with variability of a completely independent satellite-based gross primary production (GPP) data set that has been calibrated using ground-based eddy covariance

measurements. Variability of SIF and GPP over time scales of weeks to months is expected to be highly similar.

2. Data and Methods

a. Machine Learning Framework

Figure 2 shows a flow diagram of our SIF noise reduction approach as applied to either simulated or GOME-2 satellite data. We start with reflectances (or radiances) from a sensor. If the observations are simulated, noise is added according to a particular SNR model. A retrieval is then performed with the noisy spectra and will be referred to as a noisy retrieval. With real satellite data, it is beneficial to perform a bias adjustment (Joiner et al. 2020) using data over the ocean, where far-red SIF values should be close to zero, to mitigate systematic errors such as those described by Köhler et al. (2015b). In contrast to terrestrial SIF, marine SIF that escapes the ocean originates almost exclusively at red wavelengths and not at the far-red wavelengths considered here (Köhler et al. 2020). Removal of poor quality spectra is also needed for effective training. A collection of noisy, bias-adjusted, and quality controlled retrievals comprises the target for NN training. The noisy spectra are used to compute the coefficients of the leading PCs. These coefficients and optional geometrical predictors, e.g., cosines of the solar zenith angle (SZA), view zenith angle (VZA), and the phase angle (the angle between the sun and satellite) form the set of NN predictors or features.

The noise-reduced (NR) SIF retrievals may undergo a final bias adjustment that can be beneficial for real satellite data. The NR retrievals are compared with true SIF within the simulation framework. The NR retrievals can also be compared with the noisy retrievals to check for biases. This is important as there is no guarantee that the NR SIF retrievals will represent an unbiased version of the noisy retrievals. Finally, with real satellite-based SIF data, a NN may be trained using data where SIF is expected to be zero (e.g., over ocean or deserts) to predict the SIF retrieval noise for noisy or NR retrievals as a function of various parameters including SZA, VZA, and/or continuum-level reflectance/radiances (Joiner et al. 2020).

The NN training is designed to reproduce the corresponding target SIF values from the original noisy retrievals. By presenting the NN during training with only the coefficients of the leading PCs as features, the NN will not be able to reconstruct the random noise in the retrievals. So long as

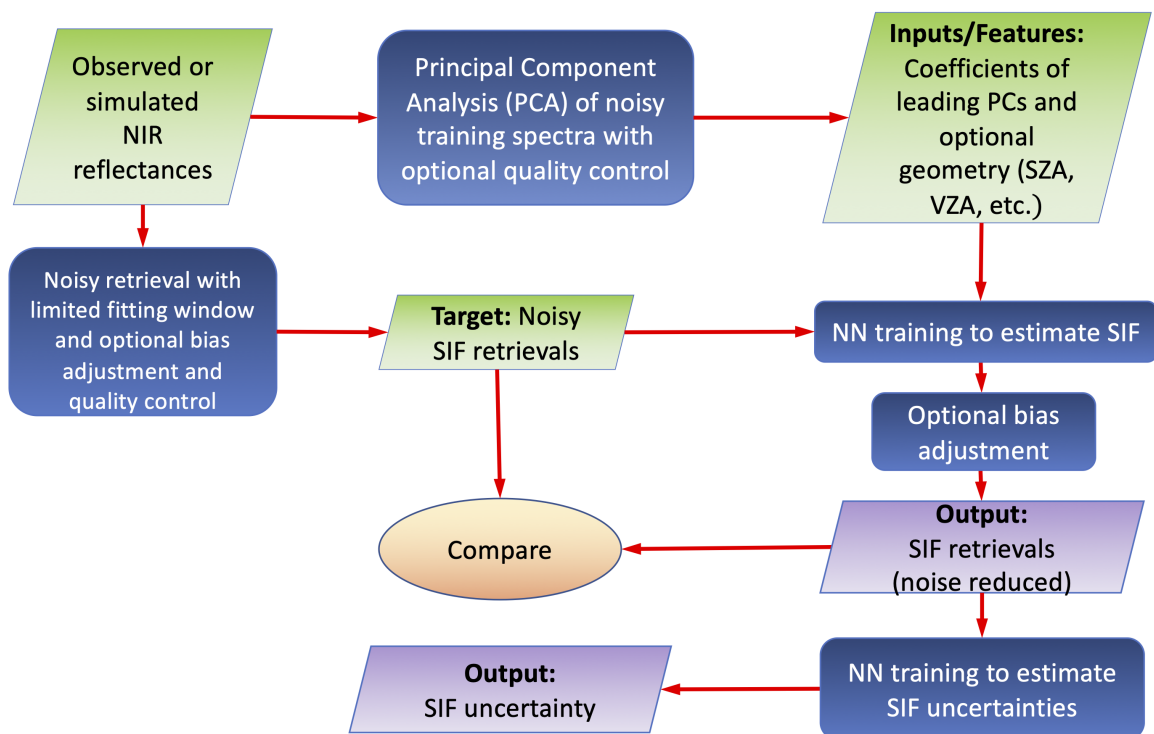


FIG. 2. Flow diagram showing steps of our SIF noise reduction algorithm. Optional bias adjustments and quality control measures are applied to the actual satellite data and are not needed with the simulated data.

sufficient information about SIF is contained in the leading PCs, our hypothesis is that the trained NN will reproduce the broad spatio-temporal variability of the retrievals.

The NR algorithm may benefit from utilizing a larger spectral fitting window than is used in the noisy retrievals. For example, current satellite-based SIF retrievals have generally avoided wavelengths within the strong O₂ A band. Non-linearity and straylight may impact radiance measurements in the deep core of this band. Our ML-based method may be able to account for these effects to utilize the SIF information within this absorption band. Our method may also be able to incorporate more spectral range across the so-called red edge (wavelengths from about 717 to 734 nm for far-red SIF retrievals) that is associated with sharp increases in reflectance owing to decreasing chlorophyll absorption. Strong H₂O features within this spectral range can be filled in by SIF emission and lead to systematic SIF retrieval errors (Parazoo et al. 2019).

For the NN architecture, we use a model with two hidden layers and a variable number of nodes in the hidden layers between 1 and 2 times the number of input features. Both inputs and outputs are scaled to give a mean of zero and standard deviation of unity. The training uses an adaptive moment estimation optimizer with a learning rate of 0.1. The activation functions for each layer are soft-sign, logistic (sigmoid), and bent identity in that order.

b. Simulated data

The simulated radiance and irradiance data are similar to those used previously (Joiner et al. 2013, 2016; Guanter et al. 2015). As in Joiner et al. (2013), radiance spectra are computed for a range of observing geometries and atmospheric and surface conditions:

VZAs of 0 and 16°, SZAs of 15, 30, 45, and 70°, middle latitude summer and winter temperature profiles, surface pressures (P_s) of 955, 980, 1005, and 1030 hPa, total water vapor column (TWVC) amounts of 0.5, 1.5, 2.5, and 4.0 cm, aerosol optical thicknesses (AOT) at 550 nm of 0.05, 0.12, 0.2, 0.3, and 0.4, and aerosol layer heights (ALH) of 700–900, 600–800, and 500–700 hPa with a typical continental aerosol model.

There are two separate simulated data sets; 1) simulated without fluorescence, consisting of ten different models of surface spectral reflectance based on soil and snow; 2) surface spectral reflectance and SIF produced with the FluorSAIL and FluorMODleaf codes (Miller et al. 2005; Jacquemoud et al. 2009; Pedrós et al. 2010). The latter has 60 different SIF values based on combinations of chlorophyll content (5, 10, 20, and 40 $\mu\text{g cm}^{-2}$), leaf area index (LAI) (0.5, 1, 2, 3, 4), and quantum efficiency (0.02, 0.05, 0.08). The atmospheric radiative transfer uses the matrix operator model (MOMO) (Fell and Fischer 2001; Preusker and Lindstrot 2009) with gaseous absorption line parameters from the high-resolution atmospheric radiance and transmittance model code (HITRAN) 2008 data set (Rothman et al. 2009).

Earthshine radiances are computed monochromatically and sampled at 0.005 nm. A solar irradiance spectrum is sampled in the same way. The spectra are convolved with instrument line shape functions of various full-width half-maximum (FWHM) values and resampled to produce data similar to those from a satellite instrument. We add noise according to a normal distribution based on a SNR model that is a function of the simulated radiance.

c. GOME-2 data

GOME-2 is a nadir-viewing spectrometer that measures Earthshine radiance and solar irradiance at wavelengths from the ultraviolet to the NIR (Munro et al. 2016). It scans cross-track providing a swath of width 1920 km in its nominal mode. GOME-2 flies aboard the European Meteorological Satellite (EUMETSAT) Polar System (EPS) MetOp mission series. So far, three instruments have flown. Here, we use data from GOME-2 on MetOp-A (GOME-2A), launched in October 2006, and on MetOp-B (GOME-2B), launched in September 2012. The drifting orbit of MetOp-A has resulted in a situation where GOME-2A lost its direct line of sight to the Sun on 26 January 2018. As a consequence, the calibration quality deteriorated along with the measurement time, and this rendered SIF measurements less useful. We focus on the overlap period between the GOME-2A and GOME-2B data sets from April 2013 through January 2018. Both satellites are in a polar orbit with an equator crossing time near 09:30 local time.

GOME-2 has four separate detector channels. We use Earthshine radiance and solar irradiance data from revision R2 in channel 4 that covers wavelengths 590–790 nm. The spectral resolution (FWHM) in this band is ~ 0.5 nm and it is sampled at approximately 0.2 nm (Munro et al. 2016). GOME-2 has a SNR in band 4 > 1000 .

3. Results

a. Results with simulated data

We use simulated data from a hypothetical instrument with a FWHM of 0.1 nm sampled every 0.03 nm. The spectral fitting window used for the noisy retrievals is 750–758 nm. This spectral range contains little atmospheric absorption, enabling a linear retrieval. Figure 3 shows the baseline SNR as a function of radiance used in the simulations.

Statistical results for retrievals with no noise and with the baseline SNR are presented as experiments (Exps.) 1 and 2, respectively, in Table 1. We then apply the noise reduction (NR) approach using an expanded fitting window of 735.5–758 nm. The input features for this experiment (and all others in this section unless otherwise specified) are coefficients of the leading 12 principal components (PCs) and cosine of the SZA. We are able to achieve a significant noise reduction; RMSE decreases by more than a factor of three as shown in Exp. 3 in Table 1.

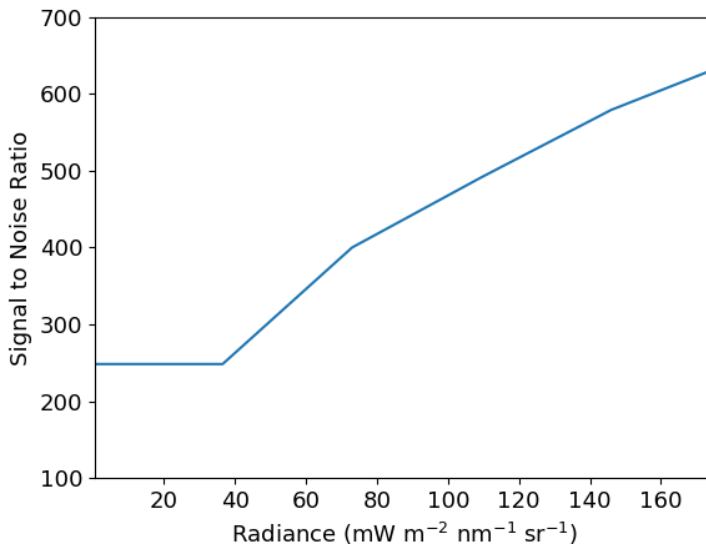


FIG. 3. Assumed nominal signal-to-noise ratio (SNR) used in simulations.

The so-called red edge comprises spectral reflectances in the approximate range of 700 to 760 nm. Within the range, reflectances for vegetated scenes rise dramatically with wavelength as a result of decreasing chlorophyll absorption. Many popular vegetation indices such as the normalized difference vegetation index (NDVI) and near-infrared reflectance of vegetation (NIR_v) make use of wavelengths on either side of the red edge. These indices are used as proxies for the total amount of green vegetation in a scene. To address the question of whether or not substantial information for the NR is coming from the red edge reflectances, we apply additional processing to the simulated reflectance spectra. First, we fit a third order polynomial to each reflectance spectrum. We then use only the fitted polynomial for the PCA. This ensures that only the broad shape of the red-edge is used for NR. The results are shown as Exp. 4. While there is a small decrease in the RMSE as compared with the noisy retrievals, the captured variance (r^2) is substantially lower than that of the original noisy retrievals. These statistics indicate that the red edge by itself is not able to reproduce the SIF variability contained in the simulated data set.

In Exp. 5 of Table 1, we subtract the fitted polynomial from the spectra before applying the PCA. This ensures that red-edge information is not utilized in the NR. In this scenario, practically all information about SIF is provided by the filling-in of solar and telluric features. Here, we achieve a substantial noise reduction, although not as much as with the unaltered spectra. These results

TABLE 1. Statistical comparison of SIF retrievals from simulations using 130227 independent observations as compared with the truth (i.e., data not used in training) including the wavelength (in nm) range used for the retrieval or noise reduction (NR) algorithms and coefficient of determination (r^2). Units of the SIF bias (mean difference with respect to the truth) and root mean squared error (RMSE) are $\text{mW m}^{-2} \text{nm}^{-1} \text{sr}^{-1}$. Unless otherwise noted, the NR uses 12 PC coefficients, includes cosine of the solar zenith angle (SZA), and does not include view zenith angle (VZA) as input features.

experiment	wavelength	r^2	bias	RMSE
1) noiseless retrieval	750.0–758.0	0.999	-0.009	0.039
2) noisy retrieval	750.0–758.0	0.797	-0.000	0.514
3) noise reduction (NR)	735.5–758.0	0.973	-0.005	0.168
4) NR, polynom. only	735.5–758.0	0.751	-0.006	0.508
5) NR, polynom. subtract.	735.5–758.0	0.951	-0.002	0.225
6) NR	740.0–758.0	0.960	-0.004	0.203
7) NR	745.0–758.0	0.916	-0.000	0.296
8) NR	750.0–758.0	0.838	-0.000	0.409
9) NR	735.5–775.0	0.974	-0.000	0.164
10) NR, 14 PCs	735.5–775.0	0.983	0.001	0.135
11) NR, 14 PCs, +VZA	735.5–775.0	0.983	-0.001	0.134
12) NR, 14 PCs, –SZA	735.5–775.0	0.981	-0.000	0.139
13) NR	750.0–775.0	0.919	-0.000	0.289
14) NR, 14PCs	750.0–775.0	0.929	-0.000	0.272
15) noisy retr., SNR \times 2	750.0–758.0	0.941	-0.006	0.256
16) NR, SNR \times 2	735.5–758.0	0.983	-0.006	0.132
17) noisy retr., SNR/2	750.0–758.0	0.496	0.011	1.023
18) NR, SNR/2	735.5–758.0	0.937	0.013	0.256
19) NR, SNR/2	750.0–775.0	0.781	0.014	0.477

indicate that the NR relies primarily on information from the Fraunhofer filling-in with a small amount of additional information from the red edge.

Experiments 6–8 use different spectral fitting windows for NR with no alteration to the original reflectance spectra. Using increasingly smaller fitting windows, as may be expected, leads to less NR. However, even the relatively narrow retrieval fitting of 750–758 nm provides a reduction in RMSE of $\sim 20\%$.

Experiments 9–14 include the O_2 A band spectral range in the NR. The 735.5–775 nm range (Exp. 9) provides NR similar to the 735.5–758.0 nm range. Increasing the number of PCs to 14 provides slightly more noise reduction (Exp. 10) than with 12 PCs. Adding the cosine of the VZA

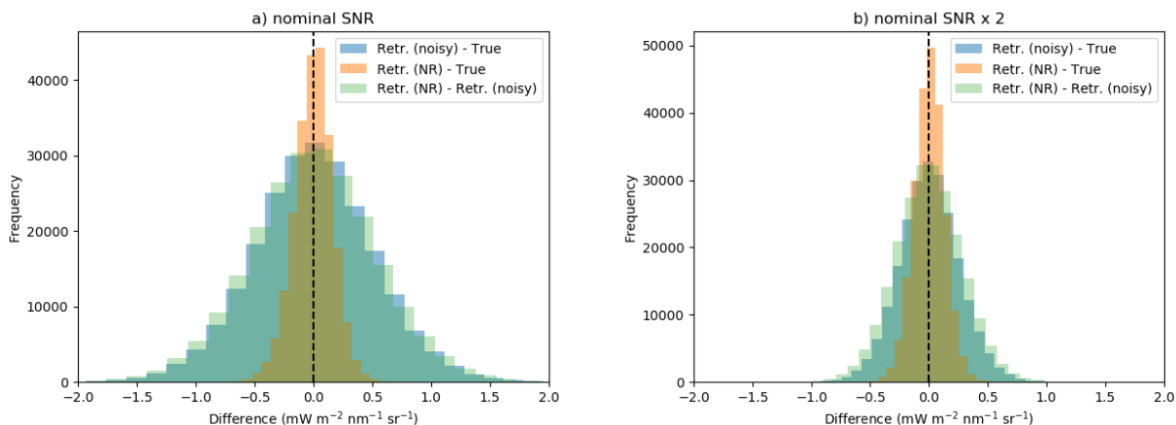


FIG. 4. Histograms of SIF retrieval errors using simulated observations with (a) nominal SNR from Fig. 3 and (b) $2 \times$ nominal SNR (noise halved).

as a predictor (Exp. 11) did not improve the results. Removing both SZA and VZA as predictors in Exp. 12 results in a very slight degradation compared with results that use SZA as a predictor. Using 750–775 nm (Exps. 13–14) reduces RMSE by about 30% as compared with 750–758 nm (Exp. 8). The use of 14 PCs as compared with 12 PCs with this spectral range provides a small additional benefit.

Experiments 15–16 similarly show results of the NR where the SNR in Figure 3 has been multiplied by a factor of two (the noise is halved). In this scenario, the noisy retrievals are much improved (RMSE about 50% lower) as compared with the nominal SNR. The amount of noise reduction is about a factor of two, somewhat less than with the nominal SNR. Histograms of the SIF retrieval errors for these experiments are shown in Figure 4 along with those from the simulations with nominal noise.

In Exps. 17–19, we repeat some of the above experiments with the SNR reduced by a factor of 2. This increases the RMSE of the noisy retrievals (Exp. 17) by a factor of about 2. The NR with the 735.5–758 nm and 750–775 nm windows (Exps. 18 and 19) reduces the RMSE by about 75% and 50%, respectively, as compared with the noisy retrievals.

b. Results with GOME-2 satellite data

1) TRAINING FREQUENCY

Here, we train a NN for each day of data collection separately for GOME-2A and GOME-2B. Separate training for each instrument allows for individual satellite instrumental artifacts to be accounted for. Frequent training may mitigate the effects of temporal variations in noise or artifacts. However, such frequent retraining adds computational cost and could lead to some unintended day to day variations.

2) BIAS ADJUSTMENT

Here, we use the bias adjustment scheme described in Joiner et al. (2020). The bias adjustment employs a similar NN model as for the NR and uses SIF retrievals over ocean as the target that are assumed to have values of zero. The five predictors are cosines of the VZA, SZA, and relative azimuth angle along with latitude and 780 nm reflectance. Note that in the original noisy retrievals, the bias adjustment scheme did not include 780 nm reflectance as a predictor. We found that better results were obtained for the NR when 780 nm reflectance is used as a bias adjustment predictor.

3) QUALITY CONTROL FILTERING

For training, we use only retrievals where $-1 < \text{SIF} < 5 \text{ mW m}^{-2} \text{ nm}^{-1} \text{ sr}^{-1}$, solar zenith angle $< 70^\circ$, and the retrieval quality value > 1 , indicating a good retrieval with effective cloud fractions $f_c < 30\%$. It should be noted that the effective cloud fraction is not the same as the geometrical cloud fraction and is applied in the context of the independent pixel approximation in which a pixel radiance is modeled as the sum of clear and cloudy subpixels, where the cloudy subpixel is modeled as an opaque surface with reflectance of 0.8. We estimate $f_c = (R_{\text{TOA}} - R_s) / (0.8 - R_s)$, where R_s is the surface albedo, and R_{TOA} is the top-of-atmosphere reflectance. We remove data where the reflectance at 680 nm > 0.6 (assumed to be over snow or ice) and at latitudes 60°S – 90°S .

Positive SIF retrieved values in the southern part of the Arabian peninsula are attributed to luminescence of the surface rocks (Köhler et al. 2021). We therefore exclude data covering 10°N – 30°N and 45°E – 60°E from the training set. Removing retrievals in the area improved SIF retrieval fits to the independent data and reduced the false positive terrestrial SIF values in this region in the NR retrievals.

An additional two-step check eliminates spectra that are not well reconstructed using leading PCs. Problematic spectra can include those affected by saturation or non-linearity in bright scenes, large amounts of stray light, severe noise in the South Atlantic Anomaly (SAA), and eclipses (Gorkavyi et al. 2021). In step 2, we reconstruct each spectrum using 28 leading PCs from step 1. The reconstruction errors (differences between the observed and reconstructed spectra) are used to identify problematic spectra. For each spectrum i , we compute the maximum absolute value $|\epsilon_{\max}|$ and the standard deviation (σ_i) of the reconstruction error over all wavelengths. We retain only spectra for a second PCA for which 1) $|\epsilon_{\max}| < 5\sigma_{\max}$, where σ_{\max} is the standard deviation of $|\epsilon_{\max}|$ computed over all spectra and 2) $\sigma_i < 5\sigma_{\sigma_i}$, where σ_{σ_i} is the standard deviation of σ_i computed over all spectra. This check removes $\sim 0.5\%$ of spectra.

The final sample of data used for NN training includes all data over land passing the above-mentioned quality control criteria as well as ocean data with an additional check that $|\text{SIF}| < 0.75 \text{ mW m}^{-2} \text{ nm}^{-1} \text{ sr}^{-1}$. We found frequent cases of clear sky pixels over ocean adjacent to cloudy pixels where we hypothesize that three dimensional (3D) radiative cloud effects contribute light from outside the footprint that can fill in solar Fraunhofer lines, leading to a false SIF signals. Maintaining this check on SIF over ocean removes such cases from the training set. The cloud 3D effects likely have a somewhat different spectral signature than SIF so that during the NN training, if eliminated from the training set, the NN does not learn to attribute them to SIF. Thus, excluding the affected observations leads to noticeable improvements over dark ocean and presumably to less obvious improvements over land.

4) SPECTRAL WINDOW AND INPUT FEATURES

To optimize the spectral fitting window and number of PCs used in the noise reduction, we examine SIF values over ocean that should tend towards zero as random and systematic errors are reduced. We report statistics of noisy and NR SIF retrievals over ocean derived from GOME-2A on 30 July 2007 in Table 2 along with statistics of the model fit of the NR to the noisy retrievals. An important objective in assessing NR performance for real data is to check random and systematic SIF errors over ocean, where the expected SIF values should be close to zero as explained above.

Using 710–758 nm for NR, the SIF standard deviation over ocean is reduced by more than a factor of four with 12 to 20 PCs. We found that more PCs are needed with real data as compared

TABLE 2. Mean and standard deviation (σ) of SIF over ocean from GOME-2A on 30 July 2007 and statistics of the model fit to the noisy bias adjusted retrievals: coefficient of determination r^2 , bias, and root mean squared error (RMSE). Units of the SIF mean, σ , bias, and RMSE are $\text{mW m}^{-2} \text{nm}^{-1} \text{sr}^{-1}$.

experiment	wavelength (nm), # PCs	mean ocean	σ ocean	r^2 ocean	bias ocean	RMSE ocean
noisy retrievals	734–758	0.103	0.618	-	-	-
NR	710–758, 12 PCs	-0.051	0.125	0.438	-0.001	0.554
NR	710–758, 15 PCs	-0.051	0.129	0.445	-0.001	0.551
NR	710–758, 20 PCs	-0.052	0.139	0.457	0.000	0.545
NR	710–775, 22 PCs	-0.049	0.131	0.454	-0.002	0.547

with the simulated data, likely because the fitting window is larger and incorporates stronger water vapor absorption; additional PCs are needed explain systematic instrumental artifacts, such as from wavelength shifts, that are absent in the simulated data. As expected, the mean SIF value also decreases in magnitude towards zero for NR retrievals, the SIF standard deviation over ocean increases with number of PCs used, and the r^2 values for the fit to the noisy data also increase.

Use of a larger wavelength range for NR that encompasses the O₂ A band with 22 PCs did not substantially improve results as compared with results that did not include the A band. This finding contrasts with the results using simulated data. It is possible that there are complex measurement errors within this deep band, such as effects of stray light or enhanced cloud 3D effects, that limit its usefulness for noise reduction.

For all subsequent GOME-2 SIF results, we use the 710–758 nm fitting window with 20 PCs. Use of 20 PCs provides both good noise reduction as well as a reasonable fit to the dynamic range of original noisy SIF data (both high and low values). Below this number, the SIF standard deviation over ocean is smaller, but the small number of SIF retrievals with large values were not captured as well. We perform further analyses below at different time scales.

5) COMPARISONS AT A DAILY TIMESCALE

Figure 5a,b shows example daily maps of noisy SIF retrievals from GOME-2B without and with bias adjustments, respectively. Figure 5c,d shows corresponding NR retrievals without and with additional bias adjustment, respectively. The NR retrievals are noticeably cleaner than the original noisy retrievals. The bias adjustment performed on the NR retrievals does not show clear signs

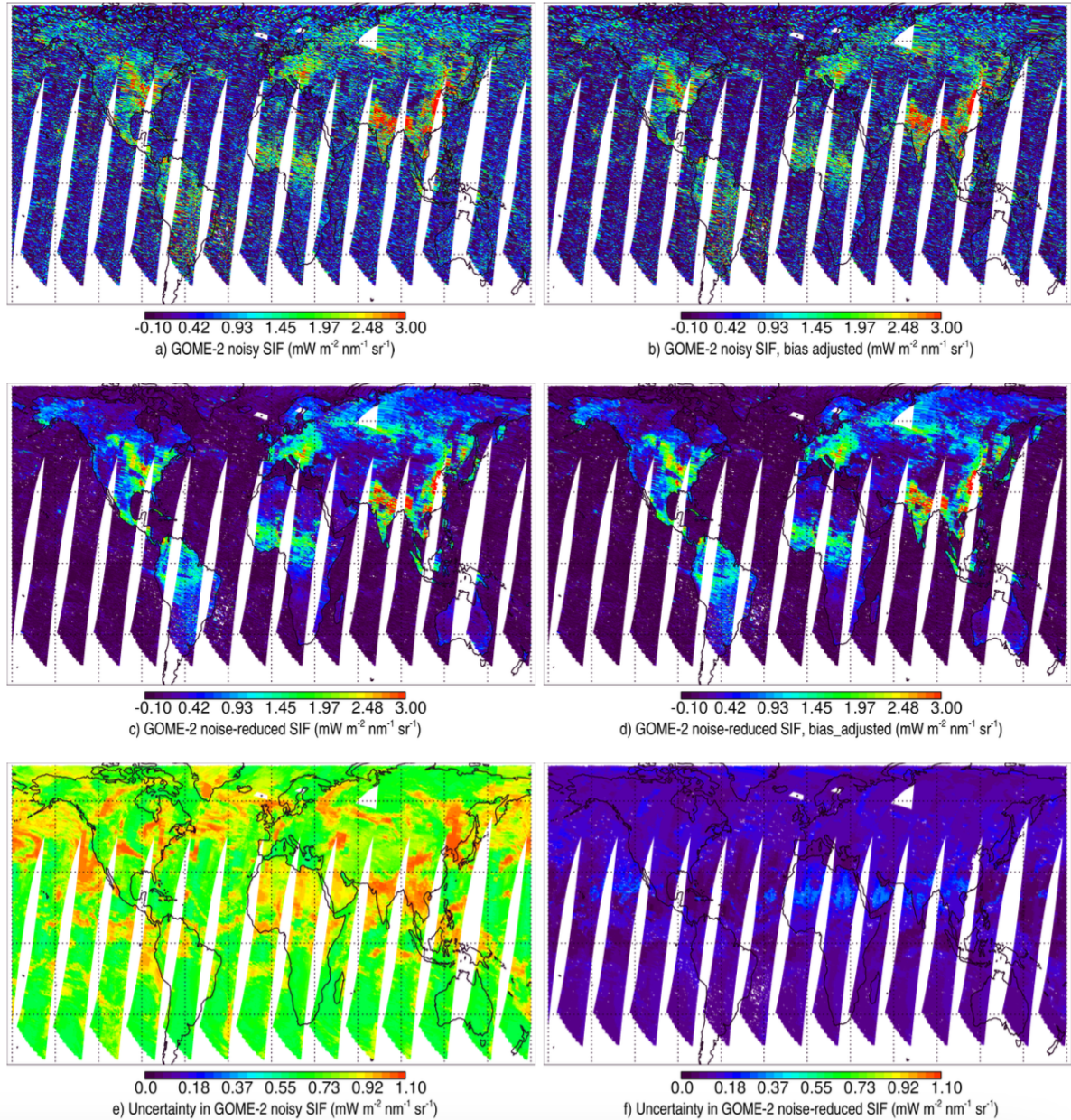


FIG. 5. Maps from GOME-2B on 28 July 2013 showing (a) noisy retrievals without bias adjustment; (b) similar to (a) but with bias adjustment; (c) similar to (a) but for noise-reduced retrievals; (d) similar to (b) but for noise-reduced retrievals; (e) estimated uncertainties for noisy retrievals; (f) similar to (e) but for noise-reduced retrievals.

of further improvement by eye, but produced slightly better statistical results over ocean and is therefore maintained in the processing chain.

Very noisy SIF retrievals are seen over the SAA region (southern Brazil extending into the Atlantic ocean) that are not present in the NR retrievals. Severely affected retrievals have been filtered out by the spectral reconstruction quality control check.

As described above, SIF retrievals over the ocean are used to train additional NNs to estimate SIF uncertainties for noisy and NR retrievals. Figure 5e,f shows estimated uncertainties from a NN trained with data over ocean. Single pixel uncertainties for the original noisy retrievals are mostly in the range of 0.6 to more than $1 \text{ mW m}^{-2} \text{ nm}^{-1} \text{ sr}^{-1}$, with the largest uncertainties corresponding to bright scenes at high latitudes. In contrast, uncertainties are below about $0.2 \text{ mW m}^{-2} \text{ nm}^{-1} \text{ sr}^{-1}$ for NR retrievals over most of the globe with only a small latitudinal band of larger errors up to about $0.5 \text{ mW m}^{-2} \text{ nm}^{-1} \text{ sr}^{-1}$ at the region of highest radiance values in the tropics.

6) COMPARISONS AT A MONTHLY TIMESCALE

Visual improvements in the NR as compared to noisy retrievals are also seen in monthly averages. Figure 6a,c shows monthly-mean gridded SIF maps from GOME-2B without and with NR, respectively, for July 2014. The monthly mean SIF values are similar for noisy and noise-reduced retrievals, although there are some subtle differences. High SIF values in the US corn belt are a bit lower in the NR SIF as compared with noisy retrievals, while NR SIF values in the tropics are somewhat higher than in the noisy retrievals. We found similar differences in other months.

Some artifacts over the ocean are removed in the NR retrievals. We found that positive SIF values in the noisy retrievals are sometimes found in clear or nearly clear sky pixels over ocean that border on cloudy regions. As discussed above, cloud 3D effects may contribute to such erroneous SIF retrievals. We found unexpected filling in of the $\text{H}\alpha$ solar line at 656 nm for some of these cases. The NN appears able to distinguish these spectral effects from those of SIF.

In the southern part of the Arabian peninsula, where luminescence from minerals in rocks occurs, positive SIF values are much reduced in NR retrievals. The spectral dependence of the luminescence was shown to be different from that of chlorophyll SIF (Köhler et al. 2021). The trained NN again appears to somewhat filter out the luminescence spectral signal.

Corresponding monthly SIF standard deviations, calculated at each gridbox using all the retrievals over the given month, are shown in Figure 6b,d. These gridbox standard deviations include both retrieval errors as well as natural variability. The monthly standard deviations are substan-

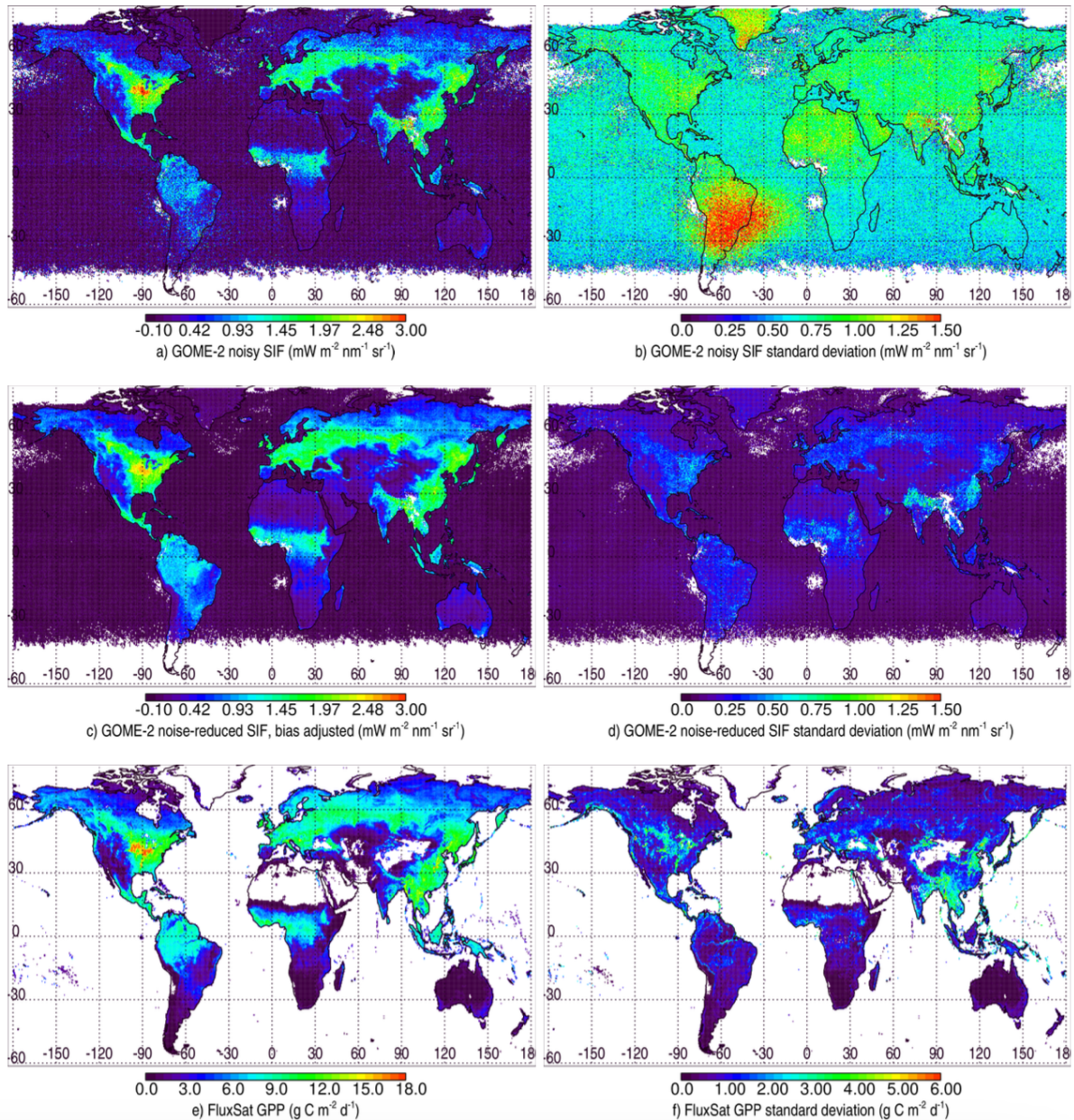


FIG. 6. Monthly averaged gridded data from GOME-2B in July 2014 at $0.5^\circ \times 0.5^\circ$ resolution (a) noisy SIF retrievals; (b) monthly gridded standard deviations from noisy retrievals; (c) similar to (a) but for noise-reduced retrievals; (d) similar to (b) but for noise-reduced retrievals; (e) Similar to (a) but gross primary production (GPP) from the FluxSat data set; (f) similar to (b) but for FluxSat GPP.

tially smaller for the NR retrievals as compared with noisy retrievals. Extremely high standard

deviations in the vicinity of the SAA are present in the noisy retrievals with values in excess of $1.5 \text{ mW m}^{-2} \text{ nm}^{-1} \text{ sr}^{-1}$, whereas these high standard deviations are absent in the NR retrievals.

As an independent validation check as to whether the more defined spatial features in the NR monthly averages are realistic, we show monthly mean and gridbox standard deviations of estimated gross primary production (GPP) from the FluxSat data set in Fig. 6e and f, respectively, at the same spatio-temporal resolution as the SIF data. FluxSat GPP is derived from MODIS reflectances calibrated with eddy covariance estimates (Joiner et al. 2018; Joiner and Yoshida 2020). It is not expected that there is not a constant scaling from SIF to GPP (Sun et al. 2023b); therefore, we should not expect a one to one correspondence between SIF and GPP. Nevertheless, spatio-temporal variations in the GOME-2 NR SIF and Fluxsat GPP show similar characteristics, providing an independent verification. For example, many fine scale spatial features, particularly at high northern latitudes, are present in both the GOME-2 SIF NR and FluxSat GPP data sets.

The contrast in standard deviations between noisy and NR SIF retrievals suggests that variability in the noisy retrievals is dominated by random errors, while variability in the NR retrievals may be more related to geophysical effects. The spatial features of variability are similar for the NR SIF retrievals and FluxSat GPP, although there are some fine scale differences. FluxSat GPP uses the clear-sky MCD43C Nadir Bidirectional Reflectance Distribution Function (BRDF)-Adjusted Reflectance (NBAR) data set that has been adjusted to nadir view to remove variability due to BRDF effects. The variability in FluxSat GPP therefore is expected to be dominated by temporal variations in vegetation structure over the month. GOME-2 SIF should show similar variability due to changes in vegetation. However, SIF should show additional variability due to its dependence on sun-satellite geometry as the scattering angles vary over a given location from orbit to orbit (Joiner et al. 2020). Gridded SIF data have also used less strict filters on cloud contamination as compared with NBAR data; effective cloud fractions of up to 30% are included in the SIF gridded data set and this contributes to gridbox variability. Therefore, we do not expect the standard deviations of SIF and GPP to be identical.

Figure 7 shows density maps of the NR versus the original noisy SIF gridbox monthly averages at $0.5^\circ \times 0.5^\circ$ resolution over land from GOME-2B for June and December of 2014. We expect to see the scatter about the 1 to 1 line with little overall bias. This has been achieved to a large degree, although again subtle differences are shown here including a slight underestimate of high SIF

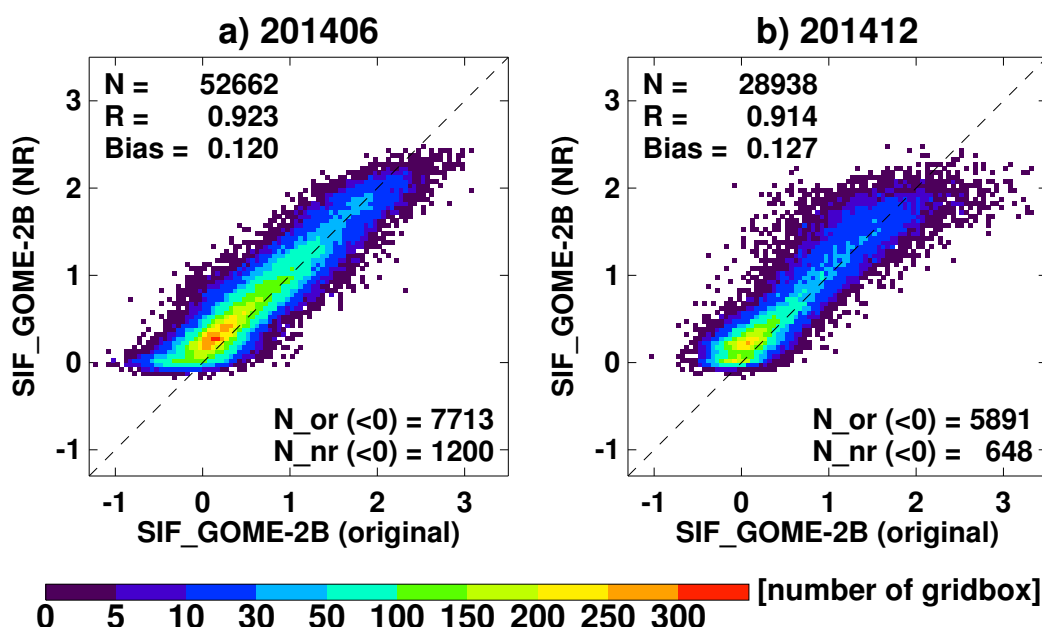


FIG. 7. Two dimensional histograms (density maps) of gridded monthly-mean noise reduced (NR) SIF retrievals versus noisy (original) SIF retrievals at $0.5^{\circ} \times 0.5^{\circ}$ resolution over land from GOME-2B for June (a) and December (b) in 2014, where colors represent the number of gridboxes, along with statistical metrics (N: number of gridboxes; R: correlation computed over all grid boxes; Bias: mean SIF difference over all grid boxes; N_or (< 0): number of gridbox averages less than zero in the original noisy data; N_nr (< 0): number of gridbox averages less than zero in the noise reduced data set; Bias and SIF units are $\text{mW m}^{-2} \text{nm}^{-1} \text{sr}^{-1}$).

values in the northern hemisphere summer months and a slight overestimation of the low values. We also see about 75% less number of negative SIF gridbox-mean values for the NR retrievals. The same data are plotted as probability distribution functions (PDFs) in Fig. A1.

7) INTER-INSTRUMENT COMPARISONS

Another means of assessing the quality of the NR retrievals is to compare results from two different instruments. Here, we compare results from GOME-2A and GOME-2B at a monthly timescale for which the effects of the different sun-satellite geometries for the two different satellites are mitigated by averaging over a range of angles. Figure 8 shows density maps of the monthly mean gridded SIF retrievals from GOME-2B versus GOME-2A in June and December of 2014

for original noisy and NR retrievals. There is improved agreement between the two instruments for NR SIF retrievals as compared with noisy retrievals. It should be noted that during this time, GOME-2A was operating in a reduced swath mode so that it experienced smaller view angles across its swath than GOME-2B that was operating in nominal swath mode. Therefore, GOME-2B observes scenes at its swath edge with higher phase angles than are experienced by GOME-2A (Joiner et al. 2020). Therefore, we may not expect perfect agreement between the two data sets.

Figure 9 shows time series of SIF monthly means computed with the original noisy and NR retrievals from GOME-2A and GOME-2B for two $0.5^{\circ} \times 0.5^{\circ}$ grid boxes. Gridbox monthly standard deviations are shown with vertical lines about the mean value. SIF values from the two instruments generally agree within their standard deviations, but with much smaller standard deviations for the NR retrievals.

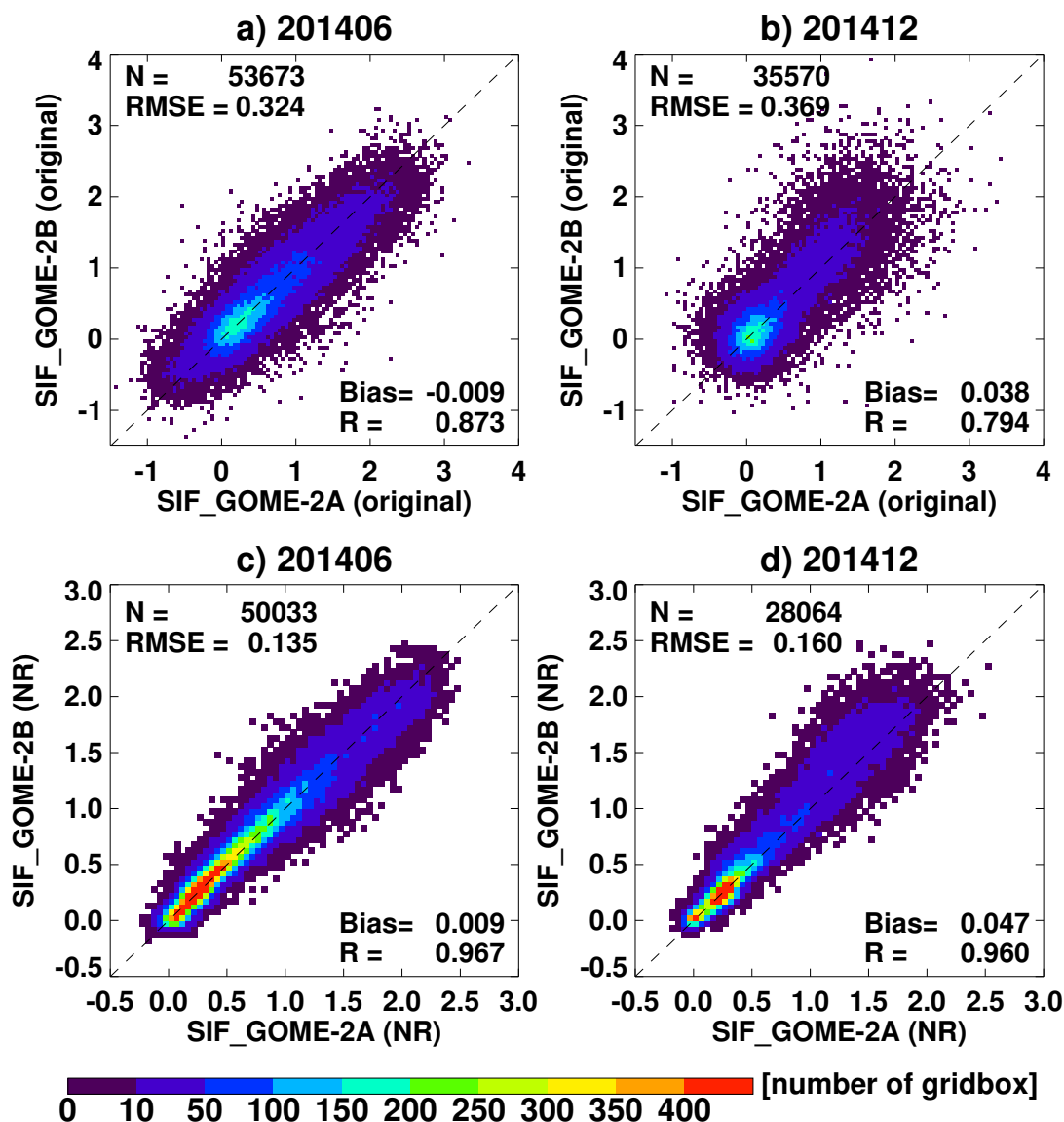


FIG. 8. Similar to Figure 7 but showing gridded monthly-mean SIF retrievals from GOME-2B versus those from GOME-2A in June and December 2014 for original (noisy) retrievals in (a) and (b), respectively, and noise reduced (NR) retrievals (c) and (d), respectively. SIF units are $\text{mW m}^{-2} \text{nm}^{-1} \text{sr}^{-1}$.

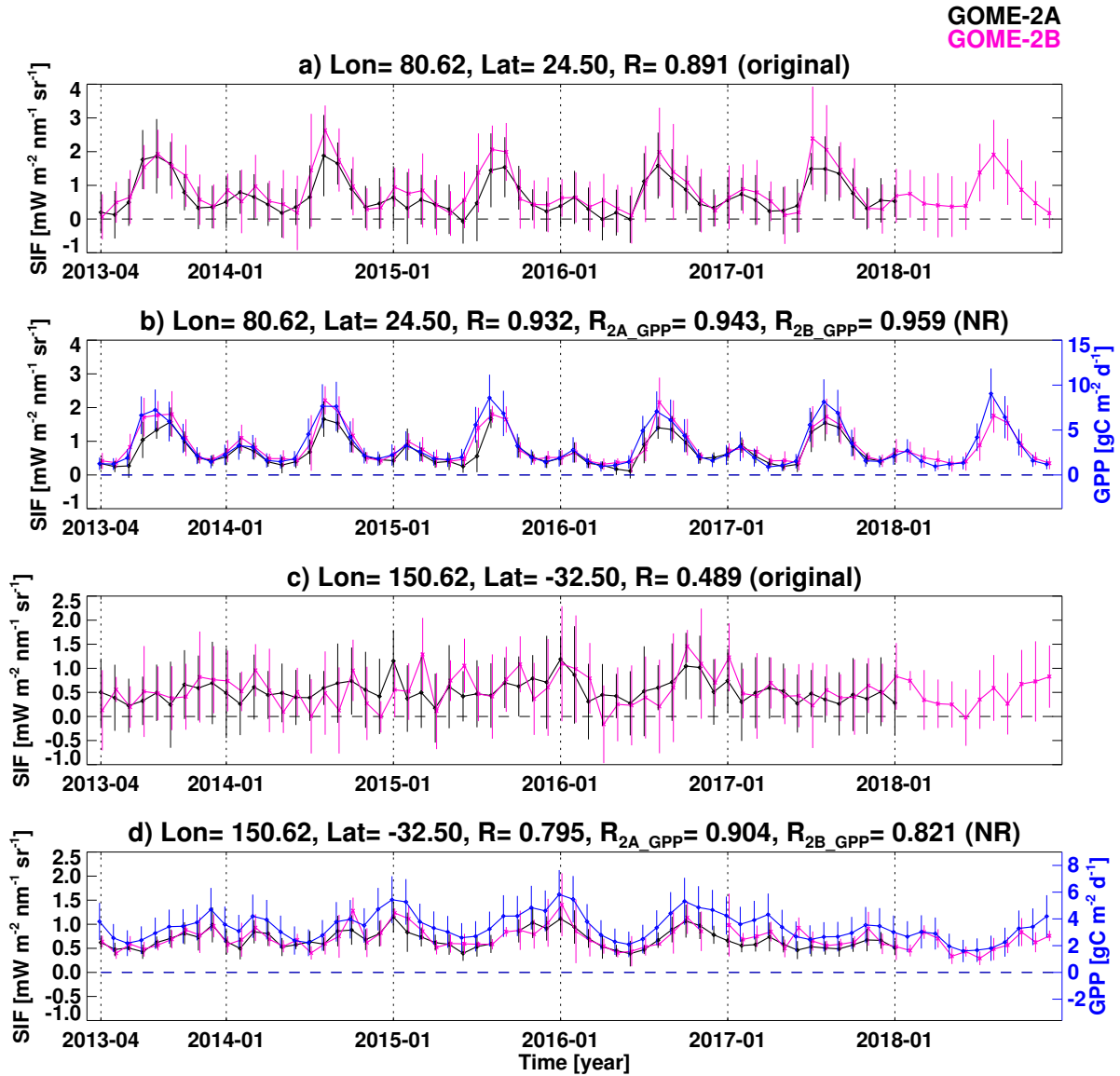


FIG. 9. Time series of GOME-2A (black lines) and GOME-2B (pink lines) monthly mean SIF from original noisy and noise reduced (NR) retrievals at selected $0.5^\circ \times 0.5^\circ$ gridboxes along with their correlations (R); gridbox standard deviations are shown with vertical lines above and below the monthly mean values. Shown with NR retrievals are time series of GPP (blue lines) from the independent FluxSat product based on MODIS reflectances aggregated to the same spatial and temporal resolution along with gridbox standard deviations. Correlations between GPP and NR GOME-2A or GOME-2B SIF monthly means are denoted R_{2A_GPP} and R_{2B_GPP} , respectively.

Seasonal cycles and interannual variability are much more apparent for the NR retrievals. There is better consistency between the two SIF data sets with the NR retrievals, lending further confidence in the method.

Time series of GPP from the independent FluxSat data set are shown for comparison with the NR retrievals and display similar seasonal and interannual variability. Correlations are higher between GPP and SIF from each of the two GOME-2 instruments than between the SIF NR retrievals from the two GOME-2 instruments. The higher correlations likely reflect lower uncertainties in the FluxSat GPP data set as compared with either SIF data set. This analysis further supports that the temporal features brought out by the NR SIF retrievals are realistic.

To assess the time series globally, Figure A2 displays maps of the gridbox SIF time series correlations between GOME-2A and GOME-2B noisy and NR retrievals for the overlap period of Apr. 2013 through Jan. 2018 with generally high correlations for NR retrievals over most moderately to highly vegetated areas. Figure A3 similarly shows maps of the gridbox correlations between NR SIF from the two GOME-2 instruments and GPP for the same time period as in Fig. A2 (Apr. 2013 to Jan. 2018); these maps show similar spatial patterns as those of the correlations between the two GOME-2 SIF data sets in Figure A2.

c. Comparison with PCA spectral noise reduction

For comparison, we performed noise reduction on the observed radiances using PCA to reconstruct spectra with leading PCs followed by SIF retrievals with the noise-reduced radiances. We applied this approach to both simulated and real GOME-2 data. With simulated data, we obtained improved results for SIF retrievals with reconstructed spectra as compared with the original noisy retrievals. However, with real GOME-2 data, we found that in order to obtain acceptable results, we required the coefficients of at least half the total number of PCs (number of wavelengths). With less PCs, biases were present. Use of a larger number of PCs resulted in less bias in SIF retrievals but with limited noise reduction.

It appears that reconstructed spectra using PCA for noise reduction is ineffective for SIF retrievals, because the very small SIF signal is spread out amongst a large number of PCs, including many that also contain a substantial amount of the random noise. For the same reason, applying our noise reduction methodology directly to the observed spectra rather than the SIF retrievals may

not work well; we would not be able to capture the total SIF signal in the radiances without using a large number of PCs and this would in turn limit noise reduction.

The good outcome with reconstructed spectra in simulated data presumably results from our inability to simulate all of the spectrally complex types of errors that can occur in real satellite data (e.g., stray light and other types of instrumental artifacts that lead to biases in the SIF retrievals). With only purely random noise in the simulation, the SIF signal is more cleanly packed into the leading PCs and therefore good results can be obtained using a smaller number of PCs.

The use of ML in our noise reduction approach allows for effective capture of the SIF signals in real satellite data with far fewer PC coefficients than is needed with reconstructed radiances. The NN effectively uses the information in fewer leading PCs to reconstruct the retrieved SIF. The use of fewer PCs leads to good reconstruction of the original signal with substantial noise reduction.

4. Conclusions

We provide a general framework for reducing the effects of random instrument noise in satellite SIF retrievals. While applied to the specific example of simulated and GOME-2 SIF data sets, the methodology should be applicable to other satellite SIF data products as well as other noisy remotely-sensed data products. The amount of improvement depends on several factors including the SNR of the original product, the spatial and temporal scales involved, and whether or not additional spectral observations (outside of the fitting window used in the original retrieval) can be effectively utilized in the approach. Different optimizations of training data sets, neural network architectures, numbers of retained PC coefficients, etc., may be needed for application to other noisy data products.

The noise reduction on a daily time scale of more than a factor of four with GOME-2 data is equivalent to averaging approximately 16 observations. We therefore achieve equivalent data quality in two days with the noise reduced data as we would have with approximately a month of the original noisy retrievals. With the substantial noise reduction, many applications of SIF data will be enabled or improved as less spatio-temporal averaging will be required for various analyses. For instance, with reduced noise, a much improved characterization of the SIF variation with orbital geometry, similar to the bi-directional reflectance distribution function (BRDF), may be possible. Complex impacts of vegetation physiology and structure on the observed top-of-canopy

or top-of-atmosphere SIF, such as characterization of the geometrical dependence of SIF, must be accounted for to effectively harness the information in SIF measurements such as extraction of information regarding physiological status (see e.g., Porcar-Castell et al. 2021; Sun et al. 2023a).

Acknowledgments. The authors thank the EUMETSAT science team who provided the level 1b GOME-2 data. This work was supported by NASA through the Making Earth Science Data Records for Use in Research Environments (MEaSUREs) program. The authors thank Michael Yan for assistance with archival of the noise reduced data sets at the Goddard Space Flight Center (GSFC) Aura Validation Data Center (AVDC).

Data availability statement. The GOME-2A and GOME-2B raw data were obtained through the US National Oceanic and Atmospheric Administration (NOAA) and are currently archived at the Comprehensive Large Array-Data Stewardship System (CLASS) at <https://www.avl.class.noaa.gov/saa/products/welcome>. The level 2 SIF products used in this work are archived at the Oak Ridge National Laboratory Distributed Active Archive Center (ORNL-DAAC) (see references within the manuscript). The authors have published the noise reduced GOME-2A and GOME-2B SIF daily and monthly-mean retrievals at the GSFC AVDC at <https://avdc.gsfc.nasa.gov> through May 2021. Simulation data, noise reduction codes, and sample input and output data sets are available (Joiner 2024).

APPENDIX

Additional figures

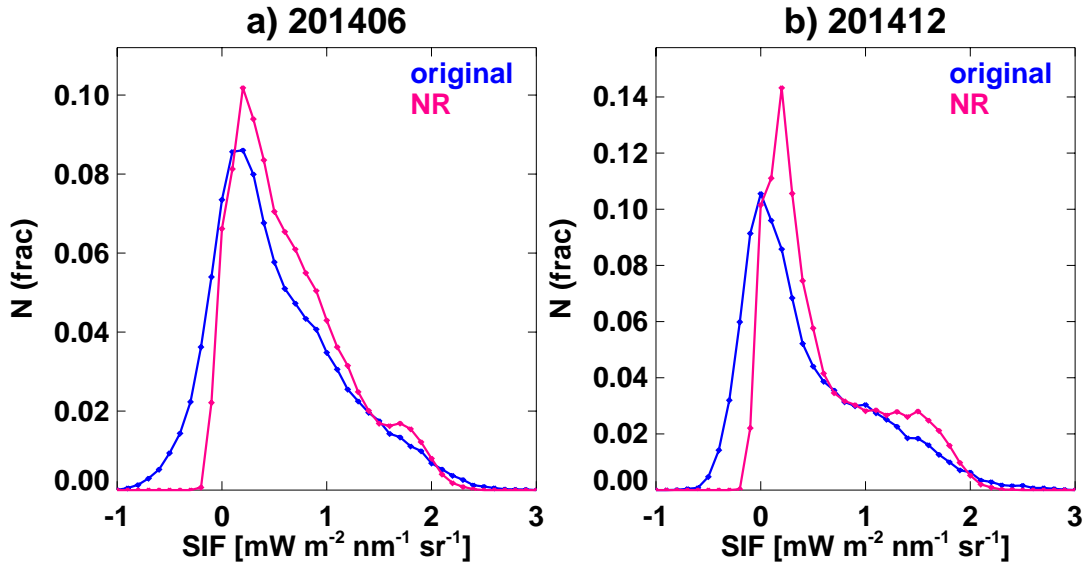


FIG. A1. PDFs, fraction of gridboxes on the y axis versus monthly mean SIF values, derived from GOME-2B data for June (a) and December (b) of 2014 corresponding to the density plots shown in Fig. 7.

Figure A1 shows PDFs of monthly mean gridded SIF from GOME-2B noisy and NR retrievals for June and December 2014. The tails of the distributions are smaller for the NR retrievals. The mode of the distributions is slightly higher (positive) for NR retrievals, whereas it is close to zero for the original noisy retrievals.

Figure A2 shows maps of gridded correlations of monthly mean SIF time series for GOME-2A and GOME-2B noisy and NR retrievals. Correlations are generally high (> 0.85) for moderately to heavily vegetated regions, except for heavily clouded tropical regions such as Amazonia. Figure A3 shows similar spatial patterns of the correlation maps between SIF from both satellites and FluxSat GPP. SIF-GPP correlations are a bit lower than the intra-satellite correlations over cloudy Amazonia which could indicate cloud contamination of the MODIS reflectances used in FluxSat and southern Australia where FluxSat has known difficulties in reproducing the GPP seasonal cycle (Joiner and Yoshida 2020). Note that during the period of overlap between GOME-2A and GOME-2B used for all maps here (Apr. 2013–Jan. 2018), GOME-2A has less coverage over polar regions due to its reduced swath.

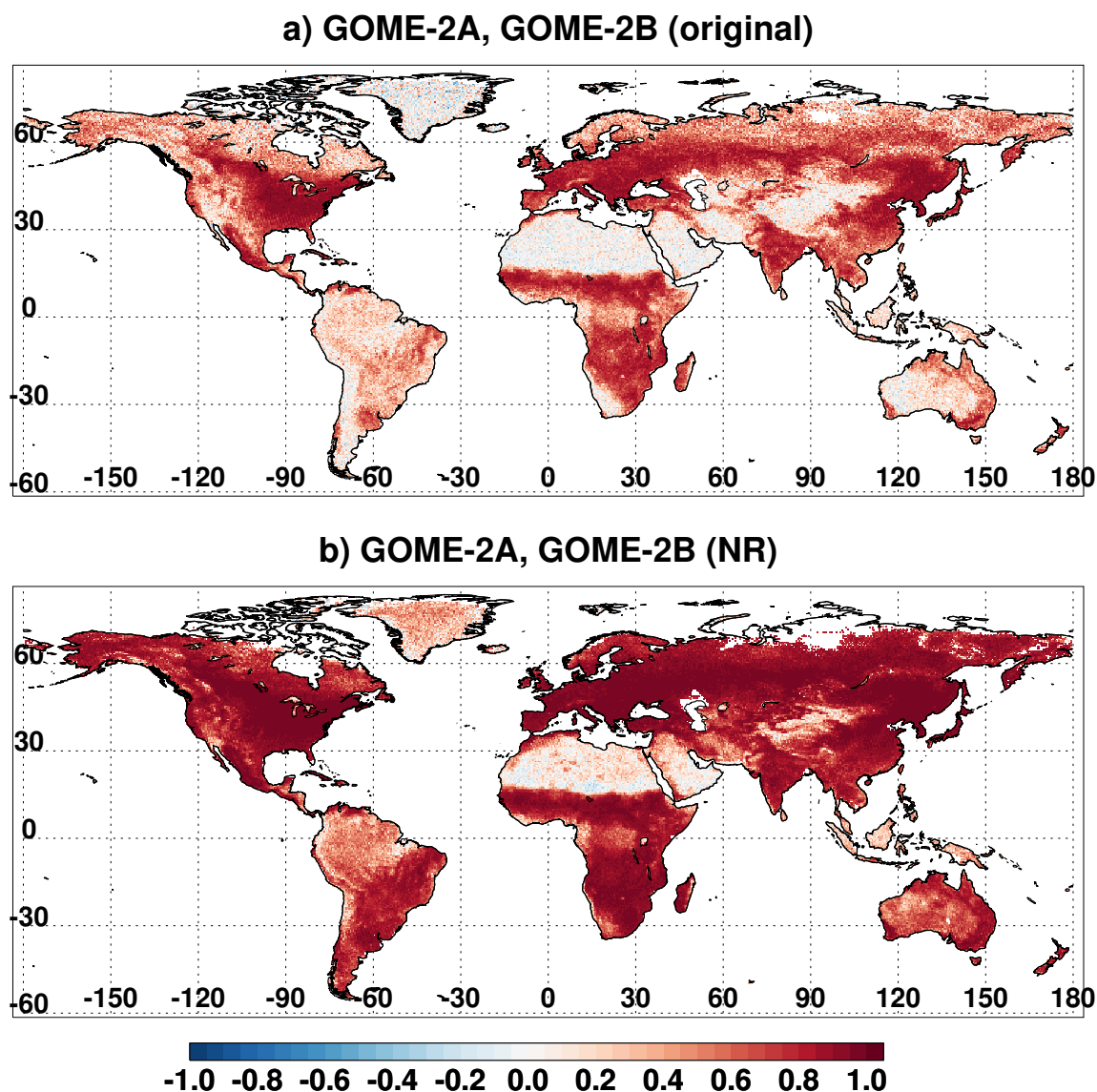


FIG. A2. Gridded correlations of monthly mean SIF time series computed during overlap periods (Apr. 2013–Jan. 2018) between GOME-2A and GOME-2B for original noisy retrievals (a) and noise reduced (NR) in (b).

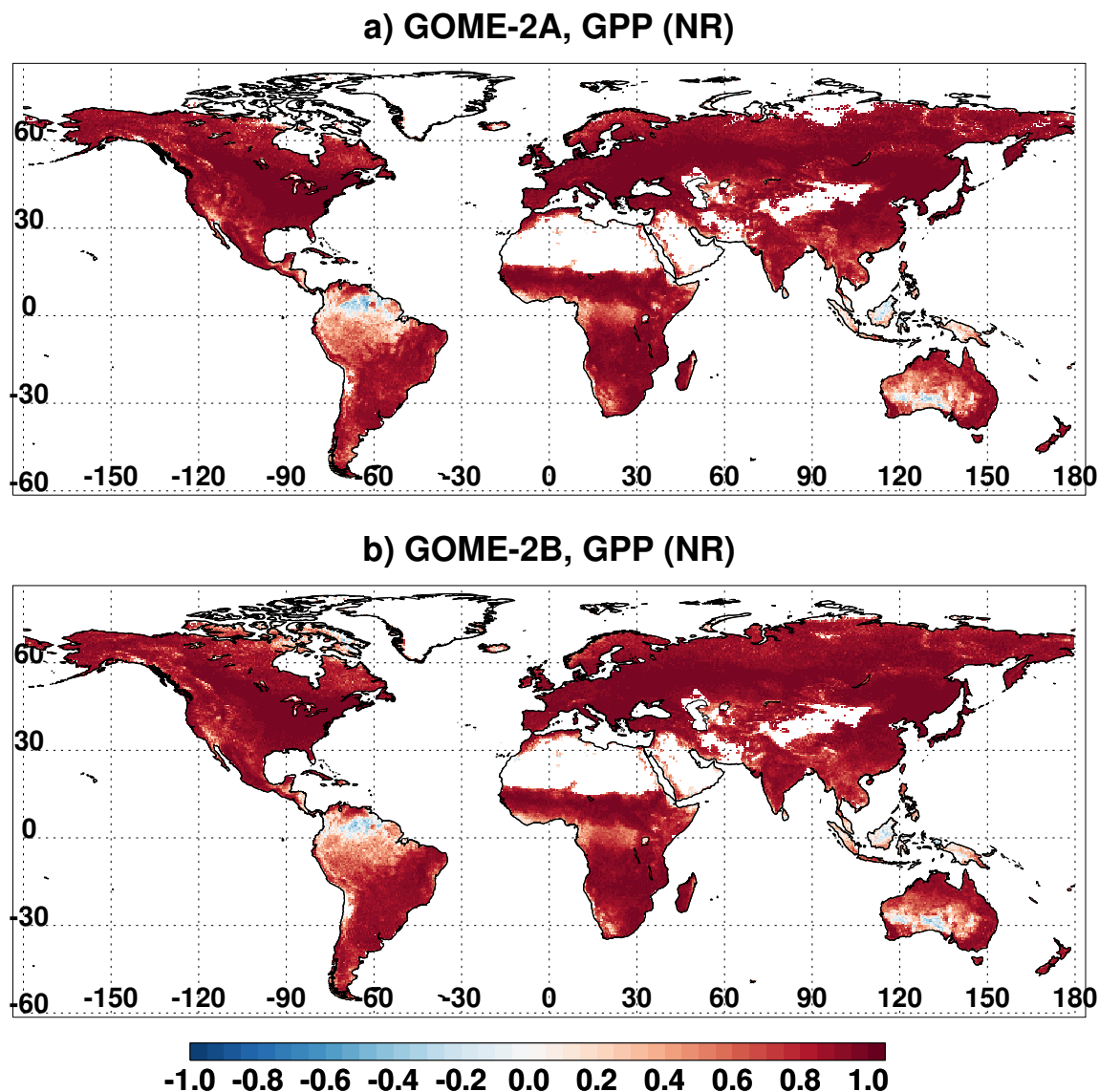


FIG. A3. Similar to Fig. A2 but showing correlations between SIF NR from GOME-2A and FluxSat GPP (a) and similarly from GOME-2B and FluxSat GPP (b). Both maps use data from Apr. 2013 to Jan. 2018.

References

- Doughty, R., T. P. Kurosu, N. Parazoo, P. Köhler, Y. Wang, Y. Sun, and C. Frankenberg, 2022: Global GOSAT, OCO-2, and OCO-3 solar-induced chlorophyll fluorescence datasets. *Earth System Science Data*, **14** (4), 1513–1529, <https://doi.org/10.5194/essd-14-1513-2022>, URL <https://essd.copernicus.org/articles/14/1513/2022/>.
- Du, S., L. Liu, X. Liu, X. Zhang, X. Zhang, Y. Bi, and L. Zhang, 2018: Retrieval of global terrestrial solar-induced chlorophyll fluorescence from TanSat satellite. *Science Bulletin*, **63** (22), 1502–1512, <https://doi.org/https://doi.org/10.1016/j.scib.2018.10.003>, URL <http://www.sciencedirect.com/science/article/pii/S2095927318304870>.
- Fell, F., and J. Fischer, 2001: Numerical simulation of the light field in the atmosphere–ocean system using the matrix-operator method. *Journal of Quantitative Spectroscopy and Radiative Transfer*, **69** (3), 351–388, [https://doi.org/https://doi.org/10.1016/S0022-4073\(00\)00089-3](https://doi.org/https://doi.org/10.1016/S0022-4073(00)00089-3), URL <https://www.sciencedirect.com/science/article/pii/S0022407300000893>.
- Frankenberg, C., A. Butz, and G. C. Toon, 2011a: Disentangling chlorophyll fluorescence from atmospheric scattering effects in O₂ A-band spectra of reflected sun-light. *Geophysical Research Letters*, **38** (3), <https://doi.org/10.1029/2010GL045896>, URL <http://dx.doi.org/10.1029/2010GL045896>, L03801.
- Frankenberg, C., and Coauthors, 2011: New global observations of the terrestrial carbon cycle from GOSAT: Patterns of plant fluorescence with gross primary productivity. *Geophysical Research Letters*, **38** (17), <https://doi.org/10.1029/2011GL048738>, URL <http://dx.doi.org/10.1029/2011GL048738>, L17706.
- Gorkavyi, N., Z. Fasnacht, D. Haffner, S. Marchenko, J. Joiner, and A. Vasilkov, 2021: Detection of anomalies in the UV–vis reflectances from the Ozone Monitoring Instrument. *Atmospheric Measurement Techniques*, **14** (2), 961–974, <https://doi.org/10.5194/amt-14-961-2021>, URL <https://amt.copernicus.org/articles/14/961/2021/>.
- Guanter, L., C. Frankenberg, A. Dudhia, P. E. Lewis, J. Gómez-Dans, A. Kuze, H. Suto, and R. G. Grainger, 2012: Retrieval and global assessment of terrestrial chlorophyll fluorescence from GOSAT space measurements. *Remote Sensing of Environment*, **121**, 236–251.

- Guanter, L., and Coauthors, 2015: Potential of the TROPOspheric Monitoring Instrument (TROPOMI) onboard the Sentinel-5 Precursor for the monitoring of terrestrial chlorophyll fluorescence. *Atmospheric Measurement Techniques*, **8** (3), 1337–1352, <https://doi.org/10.5194/amt-8-1337-2015>, URL <http://www.atmos-meas-tech.net/8/1337/2015/>.
- Guanter, L., and Coauthors, 2021: The TROPOSIF global sun-induced fluorescence dataset from the Sentinel-5P TROPOMI mission. *Earth System Science Data*, **13** (11), 5423–5440, <https://doi.org/10.5194/essd-13-5423-2021>, URL <https://essd.copernicus.org/articles/13/5423/2021/>.
- Jacquemoud, S., W. Verhoef, F. Baret, C. Bacour, P. J. Zarco-Tejada, G. P. Asner, C. François, and S. L. Ustin, 2009: PROSPECT+SAIL models: A review of use for vegetation characterization. *Remote Sensing of Environment*, **113**, S56–S66, [https://doi.org/https://doi.org/10.1016/j.rse.2008.01.026](https://doi.org/10.1016/j.rse.2008.01.026), URL <https://www.sciencedirect.com/science/article/pii/S0034425709000765>, imaging Spectroscopy Special Issue.
- Joiner, J., 2024: Solar-induced fluorescence noise reduction using simulated and real data (v1.1). machine learning based noise reduction for satellite products: application to solar-induced fluorescence retrievals using simulated and real data. Zenodo, San Francisco, CA USA, URL <https://doi.org/10.5281/zenodo.10724722>, <https://doi.org/10.5281/zenodo.10724722>.
- Joiner, J., S. Marchenko, Z. Fasnacht, L. Lamsal, C. Li, A. Vasilkov, and N. Krotkov, 2023: Use of machine learning and principal component analysis to retrieve nitrogen dioxide (NO₂) with hyperspectral imagers and reduce noise in spectral fitting. *Atmospheric Measurement Techniques*, **16** (2), 481–500, <https://doi.org/10.5194/amt-16-481-2023>, URL <https://amt.copernicus.org/articles/16/481/2023/>.
- Joiner, J., and Y. Yoshida, 2020: Satellite-based reflectances capture large fraction of variability in global gross primary production (GPP) at weekly time scales. *Agricultural and Forest Meteorology*, **291**, 108 092, [https://doi.org/https://doi.org/10.1016/j.agrformet.2020.108092](https://doi.org/10.1016/j.agrformet.2020.108092), URL <https://www.sciencedirect.com/science/article/pii/S0168192320301945>.
- Joiner, J., Y. Yoshida, L. Guanter, and E. M. Middleton, 2016: New methods for the retrieval of chlorophyll red fluorescence from hyperspectral satellite instruments: simulations

and application to GOME-2 and SCIAMACHY. *Atmospheric Measurement Techniques*, **9** (8), 3939–3967, <https://doi.org/10.5194/amt-9-3939-2016>, URL <https://www.atmos-meas-tech.net/9/3939/2016/>.

Joiner, J., Y. Yoshida, P. Köhler, C. Frankenberg, and N. Parazoo, 2019: L2 Daily Solar-Induced Fluorescence (SIF) from ERS-2 GOME, 1995-2003. ORNL DAAC, Oak Ridge, Tennessee, USA, URL <https://doi.org/10.3334/ORNLDAAAC/1758>, <https://doi.org/10.3334/ORNLDAAAC/1758>.

Joiner, J., Y. Yoshida, A. P. Vasilkov, Y. Yoshida, L. A. Corp, and E. M. Middleton, 2011: First observations of global and seasonal terrestrial chlorophyll fluorescence from space. *Biogeosciences*, **8** (3), 637–651, <https://doi.org/10.5194/bg-8-637-2011>, URL <http://www.biogeosciences.net/8/637/2011/>.

Joiner, J., Y. Yoshida, Y. Zhang, G. Duveiller, M. Jung, A. Lyapustin, Y. Wang, and C. J. Tucker, 2018: Estimation of terrestrial global gross primary production (GPP) with satellite data-driven models and eddy covariance flux data. *Remote Sensing*, **10** (9), 1346, <https://doi.org/10.3390/rs10091346>, URL <http://www.mdpi.com/2072-4292/10/9/1346>.

Joiner, J., and Coauthors, 2013: Global monitoring of terrestrial chlorophyll fluorescence from moderate-spectral-resolution near-infrared satellite measurements: methodology, simulations, and application to GOME-2. *Atmospheric Measurement Techniques*, **6** (10), 2803–2823, <https://doi.org/10.5194/amt-6-2803-2013>, URL <http://www.atmos-meas-tech.net/6/2803/2013/>.

Joiner, J., and Coauthors, 2020: Systematic orbital geometry-dependent variations in satellite solar-induced fluorescence (SIF) retrievals. *Remote Sensing*, **12** (15), <https://doi.org/10.3390/rs12152346>, URL <https://www.mdpi.com/2072-4292/12/15/2346>.

Khosravi, N., M. Vountas, V. V. Rozanov, A. Bracher, A. Wolanin, and J. P. Burrows, 2015: Retrieval of terrestrial plant fluorescence based on the in-filling of far-red fraunhofer lines using SCIAMACHY observations. *Frontiers in Environmental Science*, **3** (78), <https://doi.org/10.3389/fenvs.2015.00078>, URL <http://www.frontiersin.org/environmental/informatics/10.3389/fenvs.2015.00078/abstract>.

- Köhler, P., M. J. Behrenfeld, J. Landgraf, J. Joiner, T. S. Magney, and C. Frankenberg, 2020: Global retrievals of solar-induced chlorophyll fluorescence at red wavelengths with TROPOMI. *Geophysical Research Letters*, **47** (15), e2020GL087541, <https://doi.org/https://doi.org/10.1029/2020GL087541>, URL <https://agupubs.onlinelibrary.wiley.com/doi/abs/10.1029/2020GL087541>, e2020GL087541 10.1029/2020GL087541, <https://agupubs.onlinelibrary.wiley.com/doi/pdf/10.1029/2020GL087541>.
- Köhler, P., W. W. Fischer, G. R. Rossman, J. P. Grotzinger, R. Doughty, Y. Wang, Y. Yin, and C. Frankenberg, 2021: Mineral luminescence observed from space. *Geophysical Research Letters*, **48** (19), e2021GL095227, <https://doi.org/https://doi.org/10.1029/2021GL095227>, URL <https://agupubs.onlinelibrary.wiley.com/doi/abs/10.1029/2021GL095227>, <https://agupubs.onlinelibrary.wiley.com/doi/pdf/10.1029/2021GL095227>.
- Köhler, P., C. Frankenberg, T. S. Magney, L. Guanter, J. Joiner, and J. Landgraf, 2018b: Global retrievals of solar-induced chlorophyll fluorescence with TROPOMI: First results and intersensor comparison to OCO-2. *Geophysical Research Letters*, **45** (19), 10,456–10,463, <https://doi.org/10.1029/2018GL079031>, URL <https://agupubs.onlinelibrary.wiley.com/doi/abs/10.1029/2018GL079031>, <https://agupubs.onlinelibrary.wiley.com/doi/pdf/10.1029/2018GL079031>.
- Köhler, P., L. Guanter, and C. Frankenberg, 2015a: Simplified physically based retrieval of sun-induced chlorophyll fluorescence from GOSAT data. *IEEE Geoscience and Remote Sensing Letters*, **12** (7), 1446–1450, <https://doi.org/10.1109/LGRS.2015.2407051>.
- Köhler, P., L. Guanter, and J. Joiner, 2015b: A linear method for the retrieval of sun-induced chlorophyll fluorescence from GOME-2 and SCIAMACHY data. *Atmospheric Measurement Techniques*, **8** (6), 2589–2608, <https://doi.org/10.5194/amt-8-2589-2015>, URL <http://www.atmos-meas-tech.net/8/2589/2015/>.
- Köhler, P., L. Guanter, H. Kobayashi, S. Walther, and W. Yang, 2018: Assessing the potential of sun-induced fluorescence and the canopy scattering coefficient to track large-scale vegetation dynamics in amazon forests. *Remote Sensing of Environment*, **204**, 769 – 785, <https://doi.org/https://doi.org/10.1016/j.rse.2017.09.025>, URL <http://www.sciencedirect.com/science/article/pii/S0034425717304376>.

- Lyapustin, A., J. Martonchik, Y. Wang, I. Laszlo, and S. Korkin, 2011a: Multiangle implementation of atmospheric correction (MAIAC): 1. Radiative transfer basis and look-up tables. *Journal of Geophysical Research: Atmospheres*, **116** (D3), <https://doi.org/10.1029/2010JD014985>, URL <http://dx.doi.org/10.1029/2010JD014985>, d03210.
- Lyapustin, A., Y. Wang, I. Laszlo, R. Kahn, S. Korkin, L. Remer, R. Levy, and J. S. Reid, 2011b: Multiangle implementation of atmospheric correction (MAIAC): 2. Aerosol algorithm. *Journal of Geophysical Research: Atmospheres*, **116** (D3), <https://doi.org/10.1029/2010JD014986>, URL <http://dx.doi.org/10.1029/2010JD014986>, d03211.
- Lyapustin, A. I., Y. Wang, I. Laszlo, T. Hilker, F. G. Hall, P. J. Sellers, C. J. Tucker, and S. V. Korkin, 2012: Multi-angle implementation of atmospheric correction for MODIS (MAIAC): 3. Atmospheric correction. *Remote Sensing of Environment*, **127**, 385 – 393, <https://doi.org/10.1016/j.rse.2012.09.002>, URL <http://www.sciencedirect.com/science/article/pii/S0034425712003550>.
- Miller, J. R., and Coauthors, 2005: Development of a vegetation fluorescence canopy model. ESTEC Contract No. 16365/02/NL/FF, Final Report.
- Mohammed, G. H., and Coauthors, 2019: Remote sensing of solar-induced chlorophyll fluorescence (SIF) in vegetation: 50 years of progress. *Remote Sensing of Environment*, **231**, 111 177, <https://doi.org/10.1016/j.rse.2019.04.030>, URL <http://www.sciencedirect.com/science/article/pii/S0034425719301816>.
- Munro, R., and Coauthors, 2016: The GOME-2 instrument on the Metop series of satellites: instrument design, calibration, and level 1 data processing – an overview. *Atmospheric Measurement Techniques*, **9** (3), 1279–1301, <https://doi.org/10.5194/amt-9-1279-2016>, URL <https://www.atmos-meas-tech.net/9/1279/2016/>.
- Parazoo, N. C., C. Frankenberg, P. Köhler, J. Joiner, Y. Yoshida, T. Magney, Y. Sun, and V. Yadav, 2019: Towards a harmonized long-term spaceborne record of far-red solar-induced fluorescence. *Journal of Geophysical Research: Biogeosciences*, <https://doi.org/10.1029/2019JG005289>, URL <https://agupubs.onlinelibrary.wiley.com/doi/abs/10.1029/2019JG005289>, <https://agupubs.onlinelibrary.wiley.com/doi/pdf/10.1029/2019JG005289>.

- Pedró, R., Y. Goulas, S. Jacquemoud, J. Louis, and I. Moya, 2010: FluorMODleaf: A new leaf fluorescence emission model based on the PROSPECT model. *Remote Sensing of Environment*, **114** (1), 155–167, <https://doi.org/https://doi.org/10.1016/j.rse.2009.08.019>, URL <https://www.sciencedirect.com/science/article/pii/S0034425709002727>.
- Porcar-Castell, A., and Coauthors, 2021: Chlorophyll a fluorescence illuminates a path connecting plant molecular biology to earth-system science. *Nature Plants*, **7** (8), 998–1009, <https://doi.org/10.1038/s41477-021-00980-4>, URL <https://doi.org/10.1038/s41477-021-00980-4>.
- Preusker, R., and R. Lindstrot, 2009: Remote sensing of cloud-top pressure using moderately resolved measurements within the oxygen A band—A sensitivity study. *Journal of Applied Meteorology and Climatology*, **48** (8), 1562 – 1574, <https://doi.org/https://doi.org/10.1175/2009JAMC2074.1>, URL <https://journals.ametsoc.org/view/journals/apme/48/8/2009jamc2074.1.xml>.
- Rasti, B., P. Scheunders, P. Ghamisi, G. Licciardi, and J. Chanussot, 2018: Noise reduction in hyperspectral imagery: Overview and application. *Remote Sensing*, **10** (3), <https://doi.org/10.3390/rs10030482>, URL <https://www.mdpi.com/2072-4292/10/3/482>.
- Rothman, L., and Coauthors, 2009: The HITRAN 2008 molecular spectroscopic database. *Journal of Quantitative Spectroscopy and Radiative Transfer*, **110** (9), 533–572, <https://doi.org/https://doi.org/10.1016/j.jqsrt.2009.02.013>, URL <https://www.sciencedirect.com/science/article/pii/S0022407309000727>.
- Sanders, A. F. J., W. W. Verstraeten, M. L. Kooreman, T. C. van Leth, J. Beringer, and J. Joiner, 2016: Spaceborne sun-induced vegetation fluorescence time series from 2007 to 2015 evaluated with Australian flux tower measurements. *Remote Sensing*, **8** (11), 895, <https://doi.org/10.3390/rs8110895>, URL <http://www.mdpi.com/2072-4292/8/11/895>.
- Schaaf, C. B., and Coauthors, 2002: First operational BRDF, albedo nadir reflectance products from MODIS. *Remote Sensing of Environment*, **83** (1), 135 – 148, [https://doi.org/http://dx.doi.org/10.1016/S0034-4257\(02\)00091-3](https://doi.org/http://dx.doi.org/10.1016/S0034-4257(02)00091-3), URL <http://www.sciencedirect.com/science/article/pii/S0034425702000913>.

- Sun, Y., C. Frankenberg, M. Jung, J. Joiner, L. Guanter, P. Köhler, and T. Magney, 2018: Overview of Solar-Induced chlorophyll Fluorescence (SIF) from the Orbiting Carbon Observatory-2: Retrieval, cross-mission comparison, and global monitoring for GPP. *Remote Sensing of Environment*, **209**, 808–823, <https://doi.org/10.1016/j.rse.2018.02.016>, URL <https://www.sciencedirect.com/science/article/pii/S0034425718300221>.
- Sun, Y., and Coauthors, 2017: OCO-2 advances photosynthesis observation from space via solar-induced chlorophyll fluorescence. *Science*, **358** (6360), eaam5747, <https://doi.org/10.1126/science.aam5747>, URL <http://science.sciencemag.org/content/358/6360/eaam5747>, <http://science.sciencemag.org/content/358/6360/eaam5747.full.pdf>.
- Sun, Y., and Coauthors, 2023a: From remotely sensed solar-induced chlorophyll fluorescence to ecosystem structure, function, and service: Part I-Harnessing theory. *Global Change Biology*, <https://doi.org/10.1111/gcb.16634>, URL <https://onlinelibrary.wiley.com/doi/abs/10.1111/gcb.16634>, <https://onlinelibrary.wiley.com/doi/pdf/10.1111/gcb.16634>.
- Sun, Y., and Coauthors, 2023b: From remotely-sensed SIF to ecosystem structure, function, and service: Part II - Harnessing data. *Global Change Biology*, <https://doi.org/10.1111/gcb.16646>, URL <https://onlinelibrary.wiley.com/doi/abs/10.1111/gcb.16646>, <https://onlinelibrary.wiley.com/doi/pdf/10.1111/gcb.16646>.
- Thakur, R. S., S. Chatterjee, R. N. Yadav, and L. Gupta, 2021: Image de-noising with machine learning: A review. *IEEE Access*, **9**, 93 338–93 363, <https://doi.org/10.1109/ACCESS.2021.3092425>.
- van Schaik, E., and Coauthors, 2020: Improved SIFTER v2 algorithm for long-term GOME-2A satellite retrievals of fluorescence with a correction for instrument degradation. *Atmospheric Measurement Techniques*, **13** (8), 4295–4315, <https://doi.org/10.5194/amt-13-4295-2020>, URL <https://amt.copernicus.org/articles/13/4295/2020/>.
- Wang, X., Z. Luo, W. Li, X. Hu, L. Zhang, and Y. Zhong, 2022: A self-supervised denoising network for satellite-airborne-ground hyperspectral imagery. *IEEE Transactions on Geoscience and Remote Sensing*, **60**, 1–16, <https://doi.org/10.1109/TGRS.2021.3064429>.

Yao, L., and Coauthors, 2022: Retrieval of solar-induced chlorophyll fluorescence (SIF) from satellite measurements: comparison of SIF between TanSat and OCO-2. *Atmospheric Measurement Techniques*, **15** (7), 2125–2137, <https://doi.org/10.5194/amt-15-2125-2022>, URL <https://amt.copernicus.org/articles/15/2125/2022/>.